NASI-648

IN-08-CR

021691

AEROSTRUCTURAL VORTICAL FLOW INTERACTIONS WITH APPLICATIONS TO F/A-18 AND F-117 TAIL BUFFET

Osama A. Kandil, Steven J. Massey and Essam F. Sheta
Aerospace Engineering Department
Old Dominion University, Norfolk, VA 23529

HIGH-ANGLE-OF-ATTACK TECHNOLOGY CONFERENCE
NASA Langley Research Center, Hampton, VA
September 17-19, 1996

AEROSTRUCTURAL VORTICAL FLOW INTERACTIONS WITH APPLICATIONS TO F/A-18 and F-117 TAIL BUFFET

Osama A. Kandil[1], Steven J. Massey[2] and Essam F. Sheta[3]
Aerospace Engineering Department
Old Dominion University, Norfolk, VA 23529

SUMMARY

The buffet response of the flexible twin-tail configuration of the F/A-18 and a generic F-117 aircraft are computationally simulated and experimentally validated. The problem is a multidisciplinary, one which requires the sequential solution of three sets of equations on a multi-block grid structure. The first set is the unsteady, compressible, full Navier-Stokes equations. The second set is the aeroelastic equations for bending and torsional twin-tail responses. The third set is the grid-displacement equations which are used to update the grid coordinates due to the tail deflections. The computational models consist of a 76°-swept back, sharp edged delta wing of aspect ratio of one and a swept-back F/A-18 or F-117 twin-tail. The configuration is pitched at 30° angle-of-attack. The problem is solved for the initial flow conditions with the twin tails kept rigid. Next, the aeroelastic equations of the tails are turned on along with the grid-displacement equations to solve for the bending and torsional tails responses due to the unsteady loads produced by the vortex breakdown flow of the leading-edge vortex cores of the delta wing. Several spanwise locations of the twin tails are investigated. The computational results are validated using several existing experimental data.

INTRODUCTION

Modern combat aircraft are designed to fly and maneuver at high angles of attack and at high loading conditions. This is achieved, for example in the F/A-18 fighter, through the combination of a leading-edge extension (LEX) with a delta wing and the use of highly swept-back vertical tails. The LEX maintains lift at high angles of attack by generating a pair of vortices that trail aft over the top of the aircraft. The vortex entrains air over the vertical tails to maintain stability of the aircraft. This combination of LEX, delta wing and vertical tails leads to the aircraft excellent agility. However, at some flight conditions, the vortices emanating from the highly-swept LEX of the delta wing breakdown before reaching the vertical tails which get bathed in a wake of unsteady highly-turbulent, swirling flow. The vortex-breakdown flow produces unsteady, unbalanced loads on the vertical tails which in turn produce severe buffet of the tails and has led to their premature fatigue failure.

Experimental investigation of the vertical tail buffet of the F/A-18 models have been conducted by several investigators such as Sellers et al[1]., Erickson et al[2]., Wentz[3] and Lee and Brown[4]. These experiments showed that the vortex produced by the LEX of the wing breaks down ahead of the vertical tails at angles of attack of 25° and higher and that the breakdown flow produced unsteady loads on the vertical tails. Cole, Moss and Doggett[5] tested a rigid, 1/6 size, full-span model of an F-18 airplane that was fitted with flexible vertical tails of two different stiffness. Vertical-tail buffet response results were obtained over the range of angle of attack from −10° to +40°, and over the range of Mach numbers from 0.3 to 0.95. Their results indicated that the buffet response occured in the first bending mode, increased with increasing dynamic pressure and was larger at $M = 0.3$ than that at a higher Mach number.

An extensive experimental investigation has been conducted to study vortex-twin tail interaction on a 76° sharp-edged delta wing with vertical twin-tail configuration by Washburn, Jenkins and

---

[1]Professor, Eminent Scholar and Dept. Chair.
[2]Ph.D. Graduate Research Assistant.
[3]Ph.D. Graduate Research Assistant.

Ferman[6]. The vertical twin tails were placed at nine locations behind the wing. The experimental data showed that the aerodynamic loads are more sensitive to the chordwise tail location than its spanwise location. As the tails were moved toward the vortex core, the buffet response and excitation were reduced. Although the tail location did not affect the vortex core trajectories, it affected the location of vortex-core breakdown. Moreover, the investigation showed that the presence of a flexible tail can affect the unsteady pressures on the rigid tail on the opposite side of the model. In a recent study by Bean and Lee[7] tests were performed on a rigid 6% scale F/A-18 in a trisonic blowdown wind tunnel over a range of angle of attack and Mach number. The flight data was reduced to a non-dimensional buffet excitation parameter, for each primary mode. It was found that buffeting in the torsional mode occurred at a lower angle of attack and at larger levels compared to the fundamental bending mode.

Tail buffet studies were also conducted on a full-scale, production model F/A-18 fighter aircraft in the 80-by-120 foot wind tunnel at NASA Ames Research Center by Meyn and James[8] and Pettit, Brown and Pendleton[9]. The test matrix covered an angle of attack range of 18° to 50° and a side-slip range of -16° to 16° with wind speed up to 100 Knots. The maximum speed corresponds to a Reynolds number of 1.23×10^7 and a Mach number of 0.15.

Kandil, Kandil and Massey[10] presented the first successful computational simulation of the vertical flexible tail buffet using a delta wing-vertical tail configuration. A 76° sharp-edged delta wing has been used along with a single rectangular vertical tail which was placed aft the wing along the plane of geometric symmetry. The flexible tail was allowed to oscillate in bending modes. The flow conditions and wing angle of attack have been selected to produce an unsteady vortex-breakdown flow. Unsteady vortex breakdown of leading-edge vortex cores was captured, and unsteady pressure forces were obtained on the tail.

Kandil, Massey and Kandil[11] extended the technique used in Ref. 10 to allow the vertical tail to oscillate in both bending and torsional modes. The total deflections and the frequencies of deflections and loads of the coupled bending-torsion case were found to be one order of magnitude higher than those of the bending case only. Also, it has been shown that the tail oscillations change the vortex breakdown locations and the unsteady aerodynamic loads on the wing and tail.

Kandil, Massey and Sheta[12] studied the effects of coupling and uncoupling the bending and torsional modes for a long computational time, and the flow Reynolds number on the buffet response, of a single rectangular flexible tail. It has been shown that the coupled response produced higher deflection than that of the uncoupled response. Moreover, the response of the coupled case reached periodicity faster than that of the uncoupled case. It has also been shown that the deflections of the low-Reynolds number case were substantially lower than that of the high Reynolds number case.

In a recent paper by Kandil, Sheta and Massey[13], the buffet response of a single swept-back vertical flexible tail in transonic flow at two angles of attack (20°, 28°) has been studied. It has been shown that the aerodynamic loads and bending-torsional deflections of the tail never reached periodic response and that the loads were one order of magnitude lower than those of Ref. 12 of the subsonic flow.

In a very recent paper by the present authors[14], the buffet response of the F/A-18 twin tails were considered. The configuration consisted of a 76°-swept back, sharp-edged delta wing and a trailing-edge-extension on which the F/A-18 twin tails were attached as cantilevers. A multi-block grid was used to solve the problem for two lateral locations of the twin tails; the midspan location and the inboard location.

In this paper, we consider computational simulation and experimental validation of the flexible twin tail buffet of the F/A-18 and F-117 aircraft. Two multi-block grids are used in the computational simulation. The first consists of five blocks and is used for the twin tail F/A-18 model and the second consists of four blocks and is used for the twin tail generic F-117 model. For both models, the flexible

twin tails are allowed to oscillate in bending and torsion modes. The computed results are compared with the experimental data of Meyn and James[8] for the F/A-18 aircraft and Washburn, et. al. for the generic F-117 model.

FORMULATION

The formulation consists of three sets of governing equations along with certain initial and boundary conditions. The first set is the unsteady, compressible, full Navier-Stokes equations. The second set consists of the aeroelastic equations for bending and torsional modes. The third set consists of equations for deforming the grid according to the twin tail deflections. Next, the governing equations of each set along with the initial and boundary conditions are presented.

Fluid-Flow Equations:

The conservative form of the dimensionless, unsteady, compressible, full Navier-Stokes equations in terms of time-dependent, body-conformed coordinates ξ^1, ξ^2 and ξ^3 is given by

$$\frac{\partial \bar{Q}}{\partial t} + \frac{\partial \bar{E}_m}{\partial \xi^m} - \frac{\partial (\bar{E}_v)_s}{\partial \xi^s} = 0; m = 1-3, s = 1-3 \tag{1}$$

where

$$\xi^m = \xi^m(x_1, x_2, x_3, t) \tag{2}$$

$$\bar{Q} = \frac{1}{J}[\rho, \rho u_1, \rho u_2, \rho u_3, \rho e]^t, \tag{3}$$

$\bar{E}_m$ and $(\bar{E}_v)_s$ are the ξ^m-inviscid flux and ξ^s-viscous and heat conduction flux, respectively. Details of these fluxes are given in Ref. 10.

Aeroelastic Equations:

The dimensionless, linearized governing equations for the coupled bending and torsional vibrations of a vertical tail that is treated as a cantilevered beam are considered. The tail bending and torsional deflections occur about an elastic axis that is displaced from the inertial axis. These equations for the bending deflection, w, and the twist angle, θ, are given by

$$\frac{\partial^2}{\partial z^2}\left[EI(z)\frac{\partial^2 w}{\partial z^2}(z,t)\right] + m(z)\frac{\partial^2 w}{\partial t^2}(z,t) + m(z)x_\theta(z)\frac{\partial^2 \theta}{\partial t^2}(z,t) = N(z,t) \tag{4}$$

$$\frac{\partial}{\partial z}\left[GJ(z)\frac{\partial \theta}{\partial z}\right] - m(z)x_\theta\frac{\partial^2 w}{\partial t^2}(z,t) - I_\theta(z)\frac{\partial^2 \theta}{\partial t^2}(z,t) = -M_t(z,t) \tag{5}$$

where z is the vertical distance from the fixed support along the tail length, l_t, EI and GJ the bending and torsional stiffness of the tail section, m the mass per unit length, I_θ the mass-moment of inertia per unit length about the elastic axis, x_θ the distance between the elastic axis and inertia axis, N the normal force per unit length and M_t the twisting moment per unit length. The characteristic parameters for the dimensionless equations are c^*, a_∞^*, ρ_∞^* and c^*/a_∞^* for the length, speed, density and time; where c^* is the delta wing root-chord length, a_∞^* the freestream speed of sound and ρ_∞^* the freestream air density. The geometrical and natural boundary conditions on w and θ are given by

$$w(0,t) = \frac{\partial w}{\partial z}(0,t) = \frac{\partial^2 w}{\partial z^2}(l_t,t) = \frac{\partial}{\partial z}\left[EI(l_t)\frac{\partial^2 w}{\partial z^2}(l_t,t)\right] = 0 \tag{6}$$

$$\theta(0,t) = \frac{\partial \theta}{\partial z}(l_t,t) = 0 \tag{7}$$

3

The solution of Eqs. (4) and (5) are given by

$$w(z,t) = \sum_{i=1}^{\hat{I}} \phi_i(z) q_i(t) \tag{8}$$

$$\theta(z,t) = \sum_{j=\hat{I}+1}^{M} \phi_j(z) q_j(t) \tag{9}$$

where ϕ_i and ϕ_j are comparison functions satisfying the free-vibration modes of bending and torsion, respectively, and q_i and q_j are generalized coordinates for bending and torsion, respectively. In this paper, the number of bending modes, $\hat{I}$, is six and the number of torsion modes, $M - \hat{I}$, is also six. Substituting Eqs. (8) and (9) into Eqs. (4) and (5) and using the Galerkin method along with integration by parts and the boundary conditions, Eqs (6) and (7), we get the following equation for the generalized coordinates q_i and q_j in matrix form:

$$\begin{bmatrix} M_{11} & M_{12} \\ M_{21} & M_{22} \end{bmatrix} \begin{pmatrix} \ddot{q}_i \\ \ddot{q}_j \end{pmatrix} + \begin{bmatrix} K_{11} & 0 \\ 0 & K_{22} \end{bmatrix} \begin{pmatrix} q_i \\ q_j \end{pmatrix} = \begin{pmatrix} \hat{N}_1 \\ \hat{N}_2 \end{pmatrix} \quad \begin{array}{l} ; i = 1,2,....,\hat{I} \\ ; j = \hat{I}+1,....,M \end{array} \tag{10}$$

where

$$\left.\begin{array}{rcl} M_{11} &=& \int_0^{l_t} m\phi_r\phi_i dz \\ M_{12} &=& M_{21} = \int_0^{l_t} mx_\theta \phi_r \phi_j dz \\ M_{22} &=& \int_0^{l_t} I_\theta \phi_s \phi_j dz \end{array}\right\} \tag{11}$$

$$\left.\begin{array}{rcl} K_{11} &=& \int_0^{l_t} EI \frac{d^2\phi_r}{dz^2}\frac{d^2\phi_i}{dz^2} dz \\ K_{22} &=& \int_0^{l_t} GJ \frac{d\phi_s}{dz}\frac{d\phi_j}{dz} dz \end{array}\right\} \tag{12}$$

$$\left.\begin{array}{rcl} \hat{N}_1 &=& \int_0^{l_t} \phi_r N dz \\ \hat{N}_2 &=& \int_0^{l_t} \phi_s M_t dz \end{array}\right\} \tag{13}$$

Similar aeroelastic equations were developed for sonic analysis of wing flutter by Strganac[15]. The numerical integration of Eqs. (11-13) is obtained using the trapezoidal method with 125 points to improve the accuracy of integrations. The solution of Eq. (10), for $q_i; i = 1,2,....,\hat{I}$, and $q_j; j = \hat{I}+1,....,M$, is obtained using the Runge-Kutta scheme. Next, w, and θ are obtained from Eqs. (8) and (9).

Grid Displacement Equations:

Once w and θ are obtained at the $n+1$ time step, the new grid coordinates are obtained using simple interpolation equations. In these equations, the twin tail bending displacements, $w_{i,j,k}^{n+1}$, and their displacements through the torsion angle, $\theta_{i,j,k}^{n+1}$ are interpolated through cosine functions.

Boundary and Initial Conditions:

Boundary conditions consist of conditions for the fluid flow and conditions for the aeroelastic bending and torsional deflections of the twin tails. For the fluid flow, the Riemann-invariant boundary conditions are enforced at the inflow and outflow boundaries of the computational domain. At the plane of geometric symmetry, periodic boundary conditions is specified with the exception of grid points on the tail. On the wing surface, the no-slip and no-penetration conditions are enforced and $\frac{\partial p}{\partial n} = 0$. On the twin tail surfaces, the no-slip and no-penetration conditions for the relative velocity components are enforced (points on the tail surface are moving). The normal pressure gradient is no longer equal to zero due to the acceleration of the grid points on the tail surface. This equation becomes $\frac{\partial p}{\partial n} = -\rho \bar{a}_t.\hat{n}$, where $\bar{a}_t$ is the acceleration of a point on the tail and $\hat{n}$ is the unit normal.

Initial conditions consist of conditions for the fluid flow and conditions for the aeroelastic deflections of the twin tails. For the fluid flow, the initial conditions correspond to the freestream conditions with no-slip and no-penetration conditions on the wing and tail. For the aeroelastic deflections of the tail, the initial conditions for any point on the tail are that the displacement and velocity are zero, $w(z,0) = 0$, $\frac{\partial w}{\partial t}(z,0) = 0$, $\theta(z,0) = 0$ and $\frac{\partial \theta}{\partial t}(z,0) = 0$.

METHOD OF SOLUTION

The first step is to solve for the fluid flow problem using the vortex-breakdown conditions and keeping each of the twin tails as a rigid beam. Navier-Stokes equations are solved using the implicit, flux-difference splitting finite-volume scheme. The grid speed $\frac{\partial \xi^m}{\partial t}$ is set equal to zero in this step. This step provides the flow field solution along with the pressure difference across each of the twin tails. The pressure difference is used to generate the normal force and twisting moment per unit length of each tail. Next, the aeroelastic equations are used to obtain the twin tail deflections, $w_{i,j,k}$ and $\theta_{i,j,k}$. The grid displacement equations are then used to compute the new grid coordinates. The metric coefficients of the coordinate Jacobian matrix are updated as well as the grid speed, $\frac{\partial \xi^m}{\partial t}$. This computational cycle is repeated every time step.

COMPUTATIONAL APPLICATIONS AND DISCUSSION

Two flexible twin tail models are used in the present study. The first model consists of a twin tail-delta wing configuration for the F/A-18 aircraft and the second model consists of a twin tail-delta wing configuration for a generic F-117 model. The delta wing of the two configurations is a 76°-swept back, sharp-edged delta wing of aspect ratio of one. The two configurations are pitched at a 30° angle of attack. Next, the twin tails of each configuration along with its geometry, flow conditions, multi-block grid and aeroelastic properties are given:

F/A-18 Twin Tails:

Each one of the twin tails are of aspect ratio 1.2, a crop ratio of 0.4 and a sweep-back angle of 35° for the quarter-chord spanwise line. The chord length at the root is 0.4 and at the tip is 0.159, with a span length of 0.336. The tail airfoil section is a NACA 65-A with sharp leading edge and the thickness ratio is 5% at the root and 3% at the tip. The dihedral angle between the two tails is 40°. The spanwise distance between the two tails is 56% of the wing span. The tails are cantilevered along the edges of a trailing-edge extension of the delta wing. The Mach number and Reynolds number (based on the wing chord length) are 0.4 and 1×10^6, respectively.

A multi-block grid consisting of five blocks is used for the solution of the problem. The first block is a O-H grid for the wing and upstream region, with $101 \times 50 \times 54$ grid points in the wrap around, normal and axial directions, respectively. The second block is a H-H grid for the region between the twin tails, with $23 \times 30 \times 12$ grid points in the wrap around, normal and axial directions, respectively. The third block is a H-H grid covering the region outside the twin tails, with $79 \times 30 \times 12$ grid points in the wrap around, normal and axial directions, respectively. The fourth block is a O-H grid surrounding the second and third blocks, with $101 \times 21 \times 12$ grid points in the wrap around, normal and axial directions, respectively. The fifth block is a O-H grid for the downstream region of the twin tails, with $101 \times 50 \times 26$ grid points in the wrap around, normal and axial directions, respectively. Figure 1 shows the grid topology and a blow-up of the twin tail-delta wing configuration.

The dimensionless density and modulus of elasticity of the twin tails are 25.5 and $1.8x10^5$. The torsional rigidity of the twin tails at the root, GJ, is 2.12×10^{-2}.

Generic F-117 Twin Tails:

The twin tail-delta wing configuration consists of a 76°-swept back, sharp-edged delta wing (aspect ratio of one) and dynamically scaled flexible twin tails similar to the one used by Washburn, et. al[6]. The vertical tails are oriented normal to the upper surface of the delta wing and have a centerline sweep of 53.5°. Each tail is made of a single Aluminum spar and Balsa wood covering. The Aluminum spar has a taper ratio of 0.3 and a constant thickness of 0.001736. The chord length at the root is 0.03889 and at the tip is 0.011667, with a span length of 0.2223. The Aluminum spar is constructed from 6061-T6 alloy with density, ρ, modulii of elasticity and rigidity, E and G of 2693 kg/m^3, 6.896×10^{10} N/m^2 and 2.5925×10^{10} N/m^2; respectively. The corresponding dimensionless quantities are 2198, 4.595×10^5 and 1.727×10^5; respectively. The Balsa wood covering has a taper ratio of 0.23 and aspect ratio of 1.4. The chord length at the root is 0.2527 and at the tip is 0.058, with a span length of 0.2223. The Balsa thickness decreases gradually from 0.0211 at the tail root to 0.0111 at the tail midspan and then constant thickness of 0.0111 is maintained to the tail tip. The tail cross section is a semi-diamond shape with bevel angle of 20°. The Balsa density, modulii of elasticity and rigidity, E and G, are 179.7 kg/m^3, 6.896×10^8 N/m^2 and 2.5925×10^8 N/m^2; respectively. The corresponding dimensionless quantities are 147, 4.595×10^3 and 1.727×10^3; respectively. The tails are assumed to be magnetically suspended and the leading edge of the tail root is positioned at $x/c = 1.0$, measured from the wing apex. The freestream Mach number and Reynolds number are 0.3 and 1.25×10^6; respectively.

A multi-block grid consisting of 4 blocks is used for the solution of the problem. The first block is a O-H grid for the wing and upstream region, with $101 \times 50 \times 54$ grid points in the wrap around, normal and axial directions, respectively. The second block is a H-H grid for the inboard region of the twin tails, with $23 \times 50 \times 13$ grid points in the wrap around, normal and axial directions, respectively. The third block is a H-H grid for the outboard region of the twin tails, with $79 \times 50 \times 13$ grid points in the wrap around, normal and axial directions, respectively. The fourth block is a O-H grid for the downstream region of the twin tails, with $101 \times 50 \times 25$ grid points in the wrap around, normal and axial directions, respectively. Figure 2 shows the grid topology and a blow-up of the twin tail-delta wing configuration.

The configuration is investigated for three spanwise positions of the twin tails; the inboard location, the midspan location and the outboard location corresponding to a separation distance between the twin tails of 33%, 56% and 78% of the wing span; respectively.

Results of the F/A-18 Configuration:

Figure 3 shows three-dimensional and top views for the initial conditions with total pressure contours on the wing and twin tails along with the streamlines of the leading edge vortex cores. The initial conditions are obtained after $t = 10$ dimensionless time units ($\Delta t = 0.6 \times 10^{-3}$), with the twin tails kept rigid. It is observed that the vortex cores experience almost a symmetric breakdown on the wing starting at about 75% chordstation. Downstream of the wing, the vortex-breakdown flow is inside the region between the twin tails. A small vortex has also been observed on the outside corner of the juncture of the tail and the trailing edge extension. The static pressure contours (not shown) indicate that the static pressures on the inside surfaces of the twin tails are lower than those on the outside surfaces.

Figures 4-7 show the aeroelastic responses of the twin tails after $t = 10$ units measured from the initial conditions solution. Figure 4 shows the bending and torsion deflection responses of the left and right tails along the vertical distance z, every 2 time units. It is observed that the bending responses are in the first mode shape while the torsion responses are in the first, second and third mode shapes. Moreover, the maximum bending deflections are about two times those of the torsion responses. The bending deflections for each tail show a single sign while the torsion deflections show positive and negative signs for each tail. Figure 5 shows the history of the bending and torsion deflections and loads versus time of the tail tip point and mid point for the left and right tails. Periodic responses have never been reached within the computational time of $t = 20$ units. Figures 6 and 7 show the histories of the root-bending-

moment coefficient (C_{rbm}) and the pressure coefficients on the inside (C_{pi}) and outside (C_{po}) the tail surfaces as well as the difference of the pressure difference (C_{pi-o}) versus time for the left and right tails.

Table 1 shows comparison of the root mean square of the present results for the twin tail-delta wing model of the F/A-18 with the experimental data of Meyn and James[8] and the computational results of Gee, Murman and Schiff[16] of the production model F/A-18 fighter aircraft. It should be recalled that the present model consists of a delta wing without a LEX and twin tails only, while the results of Refs. 8 and 16 are for a full F/A-18 aircraft model.

Case	C_{pi}	C_{po}	C_{pi-o}	C_{rbm}
Present CFD/Structurs Results F/A-18 Model (Left tail)	0.21	0.038	0.23	0.0252
Meyn Expiremental Data F/A-18 aircraft (As reported in Ref. 16)	0.28-0.3	0.14-0.16	0.34-0.37	0.0624-0.0814
Gee CFD Results[16] F/A-18 aircraft	0.2	0.13	0.27	0.0182

Table 1. Comparison of RMS C_p at 60% span and 45% chord, and RMS C_{rbm}.

Results of the Generic F-117 Model:

Inboard Location of Twin Tails (33 % wing span):

The spanwise distance between the two tails is 33 % of the wing span. Figure 8 shows three-dimensional and front views for the initial conditions with the surface total pressure contours and the streamlines of the vortex cores. Figure 9 shows the static pressure contours and the instantaneous streamlines in a cross flow plane at $x = 1.096$. The initial conditions are obtained after 10,000 time steps, $\Delta t = 0.001$, with the twin tails kept rigid. It is observed that the vortex cores experience an almost symmetric breakdown on the wing at about the 75% chordstation. Downstream of the wing, they are totally outside of the space between the twin tails. Smaller size vortex cores appear under the vortex breakdown flows and at the lower edges of the twin tails. These results exactly match Washburn observations. Figures 10 and 11 show the results for the twin tails undergoing uncoupled bending-torsion responses after 9,600 time steps from the initial conditions. It is observed that the breakdown shapes and locations are affected by the twin tail oscillations. The vortex breakdown is now strongly asymmetric, and the vortex breakdown flows are still outside of the space between the twin tails. These results conclusively show the upstream as well as the spanwise effects of the twin tail oscillations on the vortex breakdown flows.

Figures 12-14, show the distribution of deflection and load responses along the left and right tails every 2 time units, the history of deflection and load responses versus time and the total structural deflections and root bending moment for the left and right tails. It is observed that the bending and torsion responses are in their first and second mode shapes. The frequencies of the bending deflections are less than one-half those of the torsion deflections. The normal forces are out of phase of the bending deflections while the torsion moments are in phase with the torsion deflections. The total tail responses are in first, second and third mode shapes. Periodic responses have not been reached within the computational time covered (20,000 time steps = 10 dimensionless time units).

Midspan Location of Twin Tails (56% wing span):

The results of this case are presented in Figs. 15-21. Figures 15-18 show that the tails cut through the vortex breakdown of the leading-edge vortex cores, which are also asymmetric. Figure 18 shows that the bending deflections are lower than those of the inboard case while the torsional deflections are substantially lower than those of the inboard case. Moreover, Fig. 18 shows that the bending and torsion deflections have a single sign for the left and right tails (all are positive or all are negative). Figure 20 shows that both bending and torsion deflections are out of phase of the normal force and twisting moment loads. The total deflections of Fig. 21 show the same trend. The root bending moments of Fig. 21 are also lower than those of the inboard case.

Outboard Location of Twin Tails (78% wing span):

Figures 22-26 show the results of this case. Figures 22 and 23 show that the space between the twin tails include larger portion of the vortex breakdown flow of the leading-edge vortex cores, than that of the midspan case. The vortex breakdown flow is also asymmetric. The vortical flow on the lower outside surfaces of the twin tails is larger than any of the above two cases. Figures 24-26 show that the bending and torsion deflections are lower than those of the midspan case. They also show that both bending and torsion deflections are out of phase of the bending and torsional loads. The frequencies of the bending deflections are still smaller than those of the torsion deflections. All these observations are in very good agreement with those of Washburn, et. al. (Ref 6). Figures 27-29 show the histories of the lift and drag coefficients versus time for the inboard, midspan and outboard locations. It is observed that the loss in CL is the largest for the inboard location case.

Table 2. shows a comparison of the present results of the mean root bending moment for flexible twin tails and the lift coefficient with rigid twin tails with those of Washburn, et. al. (Ref 6), experimental data.

Parameter	Position	FTNS3D	WASHBURN
Mean Root Bending Moment With Flexible Tails	Inboard	5.62×10^{-5}	7.43×10^{-5}
	Midspan	4.22×10^{-5}	6.05×10^{-5}
	Outboard	3.62×10^{-5}	5.70×10^{-5}
Lift Coefficient With Rigid Tails	Inboard	1.0423	1.17
	Midspan	1.0515	1.12
	Outboard	1.0674	1.17

Table (2) Validation of FTNS3D computational results with Washburn, et. al. experimental results[6].

CONCLUDING REMARKS

The buffet responses of the twin-tail configuration of the F/A-18 model and the generic F-117 model have been investigated computationally using three sets of equations for the aerodynamic loads, the bending and torsional deflections and the grid displacements due to the twin tail deflections. The leading-edge vortex breakdown flow has been generated using a 76°-swept back sharp-edged delta wing which is pitched at 30° angle of attack. The twin tails are cantilevered at a trailing edge extension of the delta wing for the F/A-18 model and without a trailing edge extension for the generic F-117 model. One spanwise separation distance is considered for the first model and three spanwise separation distances are considered for the second model. Only, uncoupled bending-torsion

response cases are considered in this study.

The present simple model of the F/A-18 aircraft produces results which are in good agreement with the experimental and computational results of the full F/A-18 aircraft.

The present computational results of the generic F-117 model are in very good agreement with the experimental data of Washburn, et. al. generic model. It is concluded that the inboard location of the twin tails produces the largest bending-torsion loads, deflections, frequencies and root bending moments when compared with the midspan and outboard locations. The outboard location produces the least of these responses. When the twin tails cut through the vortex breakdown flow, they produces less responses due to the compensating damping effect produced by the left and right parts of the vortex breakdown flow on each tail.

Work is underway to upgrade the aeroelastic model using finite-element structural dynamics codes for shell and solid elements of the twin tails and to add an advanced turbulents model, e.g.; $k - \omega$ two equation turbulents model. Moreover, work is underway to develop passive and active control of the twin tail buffet problem.

REFERENCES

1. Sellers, W. L. III, Meyers, J. F. and Hepner, T. E., "LDV Survey Over a Fighter Model at Moderate to High Angle of Attack," SAE Paper 88-1448, 1988.

2. Erickson, G. E., Hall, R. M., Banks, D. W., Del Frate, J. H., Shreiner, J. A., Hanley, R. J. and Pulley, C. T., "Experimental Investigation of the F/A-18 Vortex Flows at Subsonic Through Transonic Speeds," AIAA 89-2222, 1989.

3. Wentz, W. H., "Vortex-Fin Interaction on a Fighter Aircraft," AIAA 87-2474, AIAA Fifth Applied Aerodynamics Conference, Monterey, CA August 1987.

4. Lee, B. and Brown, D., "Wind Tunnel Studies of F/A-18 Tail Buffet," AIAA 90-1432, 1990.

5. Cole, S. R., Moss, S. W. and Dogget, R. V., Jr., "Some Buffet Response Characteristics of a Twin-Vertical-Tail Configuration," NASA TM-102749, October 1990.

6. Washburn, A. E., Jenkins, L. N. and Ferman, M. A., "Experimental Investigation of Vortex-Fin Interaction," AIAA 93-0050, AIAA 31st ASM, Reno, NV, January 1993.

7. Bean, D. E. and Lee, B. H. K., "Correlation of Wind Tunnel and Flight Test Data for F/A-18 Vertical Tail Buffet," AIAA 94-1800-CP, 1994

8. Meyn, L. A. and James, K. D., "Full Scale Wind Tunnel Studies of F/A-18 Tail Buffet," AIAA 93-3519-CP , AIAA Applied Aerodynamics conference, Monterey, CA, August 9-11, 1993.

9. Pettit, C. L., Brown, D. L. and Pendleton, E., "Wind Tunnel Test of Full-Scale F/A-18 Twin Tail Buffet: A summary of pressure and Response Measurements," AIAA-94-3476-CP, AIAA Applied Aerodynamics conference, Colorado Springs, CO, June 1994, pp. 207-218.

10. Kandil, O. A., Kandil, H. A. and Massey, S. J., "Simulation of Tail Buffet Using Delta Wing-Vertical Tail Configuration," AIAA 93-3688-CP, AIAA Atmospheric Flight Mechanics Conference, Monterey, CA August 1993, pp. 566-577.

11. Kandil,O. A., Massey, S. J., and Kandil, H. A., "Computations of Vortex-Breakdown Induced Tail Buffet Undergoing Bending and Torsional Vibrations," AIAA 94-1428-CP, AIAA/ASME/ASCE/ASC Structural, Structural Dynamics and Material Conference, SC April 1994, pp. 977-993.

12. Kandil, O. A., Massey, S. J. and Sheta, E. F., "Structural Dynamics/CFD Interaction for Computation of Vertical Tail Buffet," International Forum on Aeroelasticity and Structural Dynamics, Royal Aeronautical Society, Manchester, U.K., June 26-28, 1995, pp. 52.1-52.14. Also published in Royal Aeronautical Journal, August/September 1996, pp. 297-303.

13. Kandil, O. A., Sheta, E. F. and Massey, S. J., "Buffet Responses of a Vertical Tail in Vortex Breakdown Flows," AIAA 95-3464-CP, AIAA Atmospheric Flight Mechanics Conference, Baltimore, MD, August 7-9, 1995, pp. 345-360.

14. Kandil, O. A., Sheta, E. F. and Massey, S. J., "Twin Tail/Delta Wing Configuration Buffet Due to Unsteady Vortex Breakdown Flow," AIAA 96-2517-CP, 14th AIAA Applied Aerodynamics Conference, New orleans, LA, June 18-20, 1996, pp. 1136-1150.

15. Straganac, T. W., "A Numerical Model of Unsteady, Subsonic Aeroelastic Behavior," NASA Technical Memorandum 100487, December 1987.

16. Gee, k., Murman, S. C. and Schiff, L. S., "Computational Analysis of F/A-18 Tail Buffet," AIAA 95-3440-CP, Atmospheric Flight Mechanics Conference, Baltimore, MD, August 1995, pp. 151-162.
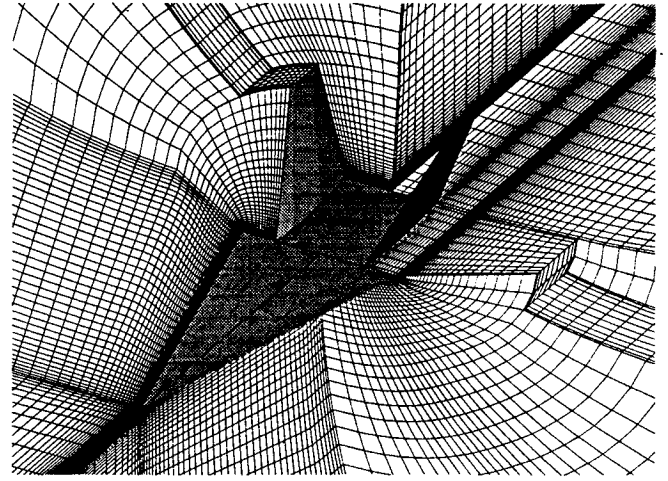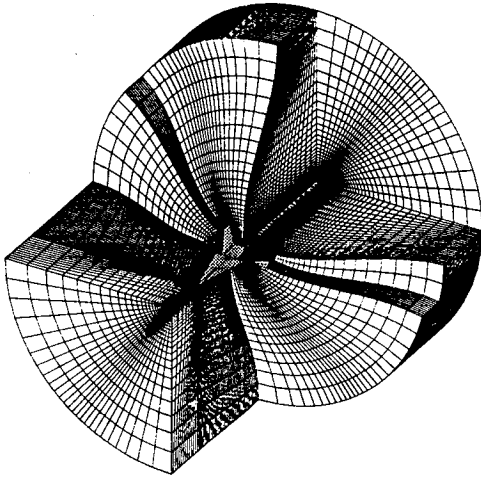
Figure 1: Three-dimensional grid topology of the twin tail-delta wing configuration (Midspan), F/A-18 model.
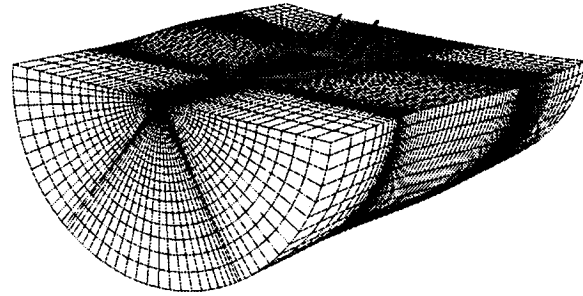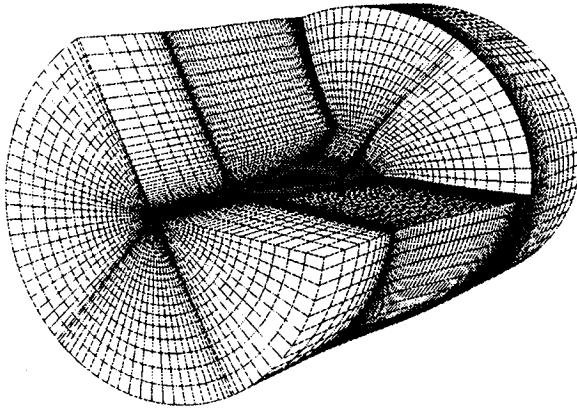
Figure 2: Three-dimensional grid topology of the twin tail-delta wing configuration (Midspan), F 117 Generic model.
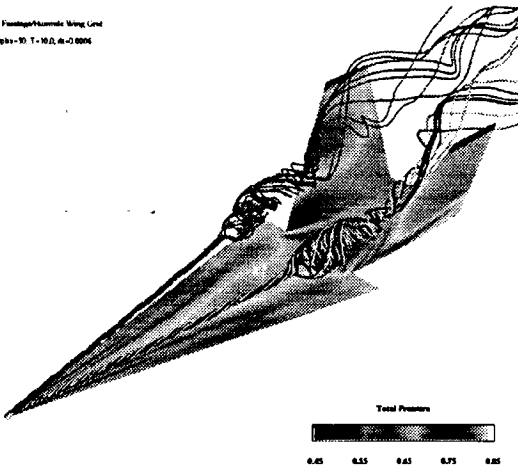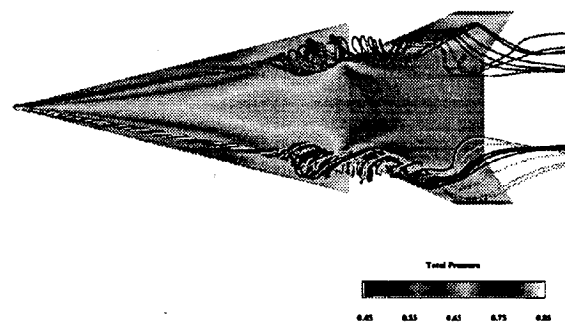
Figure 3: Three-dimensional and top views of surface pressure and vortex-cores streamlines for a rigid tail, $t = 10$, $\Delta t = 0.0006$.

(a) Left tail　　　　　　　　　　　　　　(b) Right tail
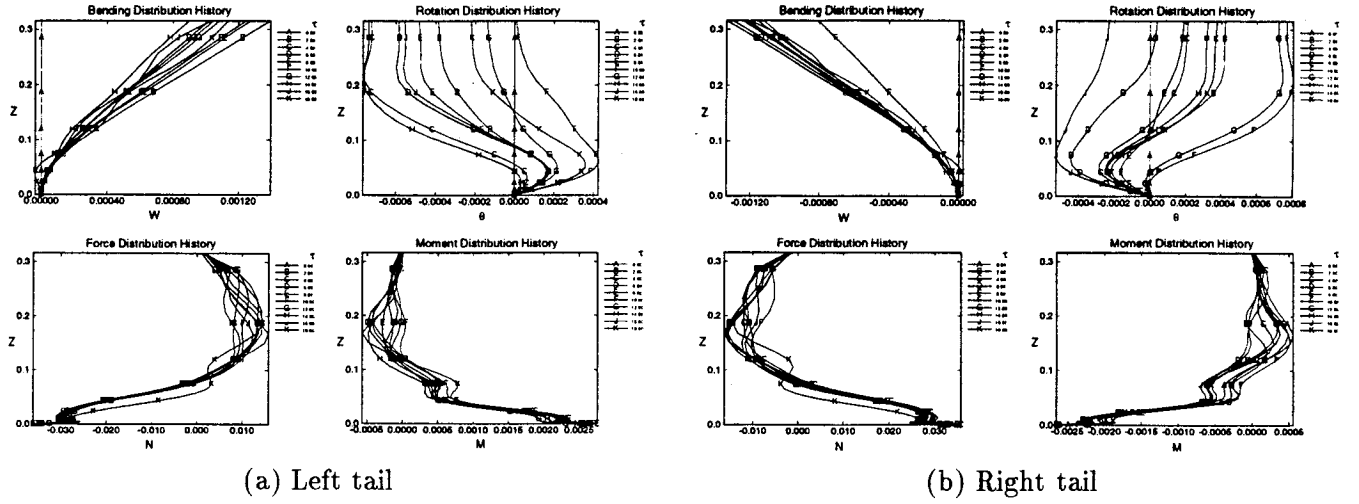
Figure 4: Distribution of the deflection and load responses for an uncoupled bending-torsion case. $M_\infty = 0.4$, $\alpha = 30^o$, $R_e = 1.00x10^6$, (Midspan position).

(a) Left tail　　　　　　　　　　　　　　(b) Right tail
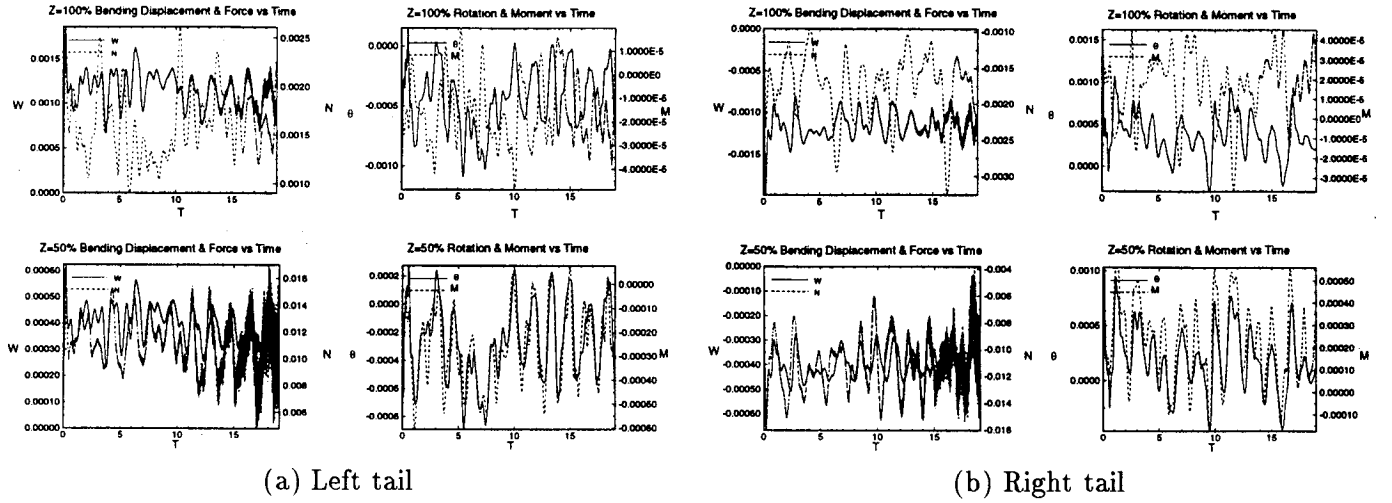
Figure 5: History of the deflection and load responses for an uncoupled bending-torsion case. $M_\infty = 0.4$, $\alpha = 30^o$, $R_e = 1.00x10^6$, (Midspan position).
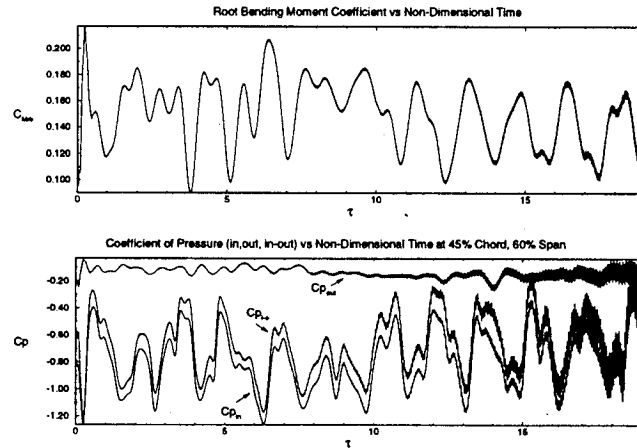
Figure 6: History of root-bending moment coefficient and surface pressure coefficients for an uncoupled bending-torsion case. $M_\infty = 0.4$, $\alpha = 30^o$, $R_e = 1.00x10^6$. Left tail (Midspan position).
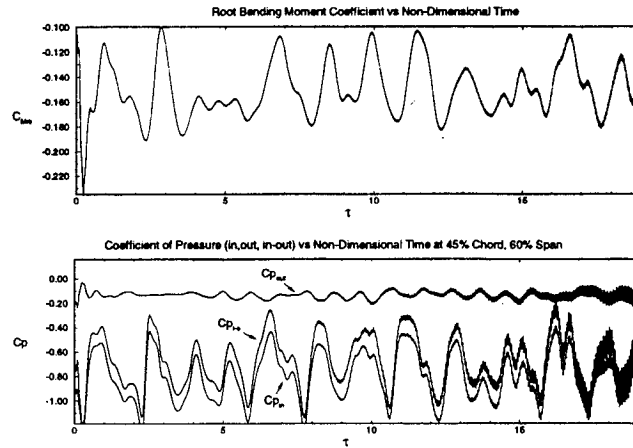
Figure 7: History of root-bending moment coefficient and surface pressure coefficients for an uncoupled bending-torsion case. $M_\infty = 0.4$, $\alpha = 30^o$, $R_e = 1.00x10^6$. Right tail (Midspan position).
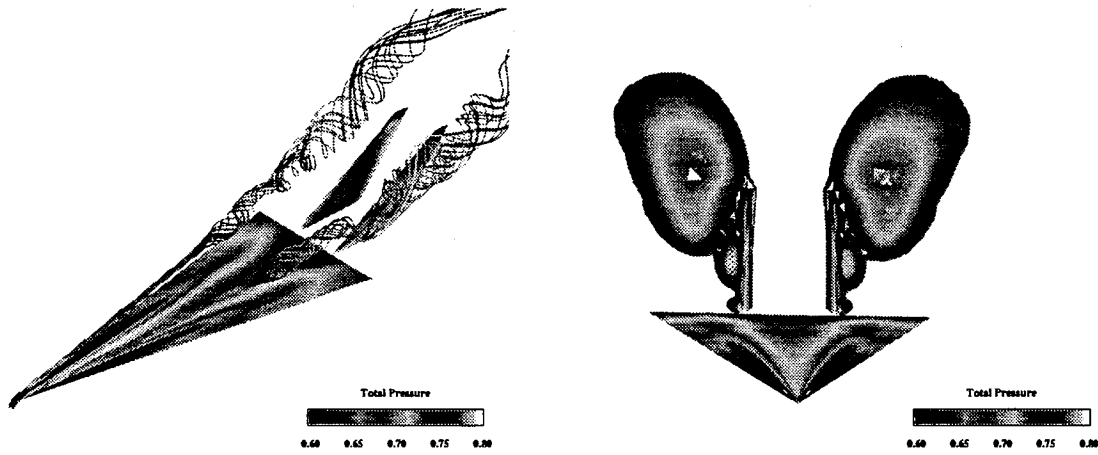
Figure 8: Three-dimensional and front views showing the total pressure on the surfaces, and the vortex-core streamlines. Initial conditions (Inboard position).
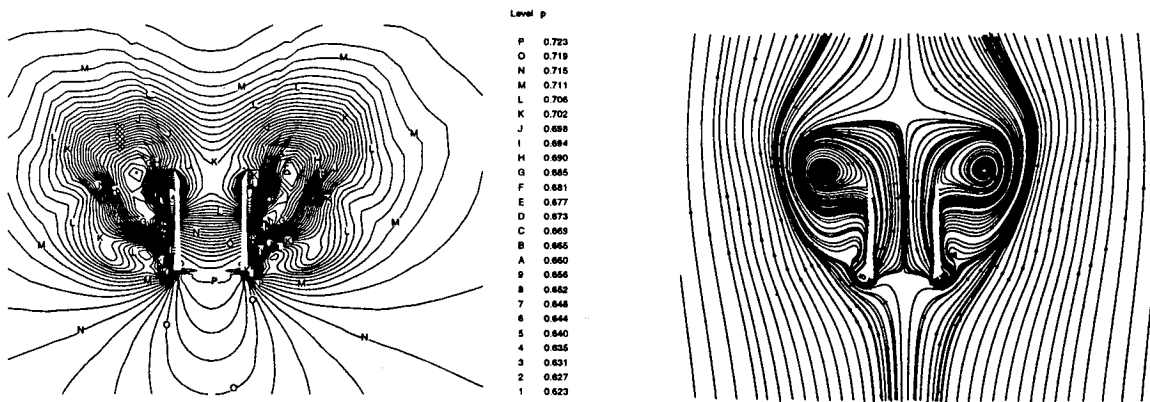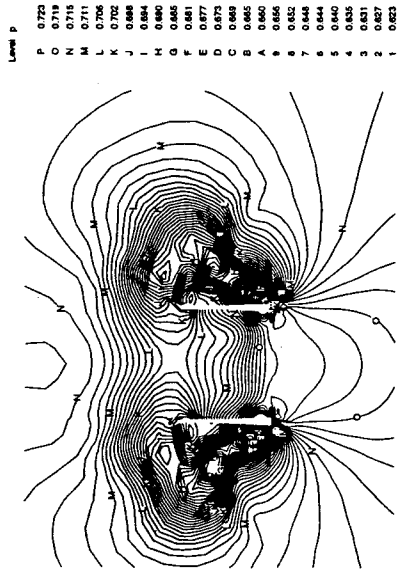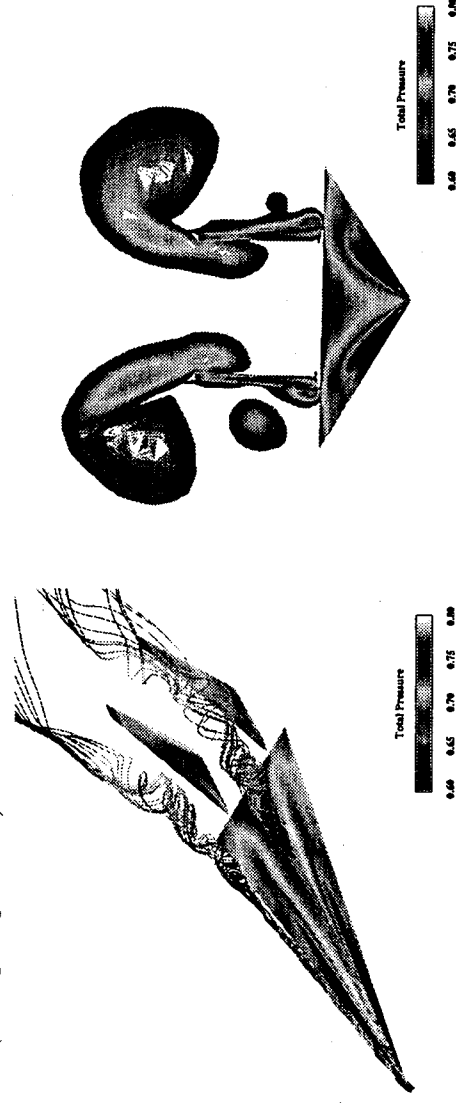

Figure 9: Initial conditions for static pressure and instantaneous streamlines in a cross-flow plane, $x = 1.096$ (Inboard position).

13
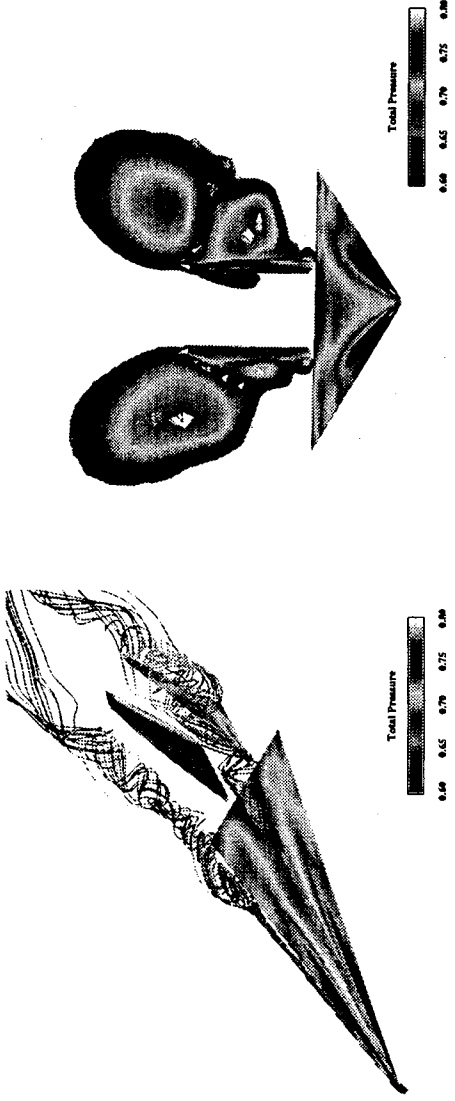
Figure 10: Three-dimensional and front views showing the total pressure on the surfaces, and the vortex-core streamlines. Uncoupled case after $it = 9,600$ (Inboard position).
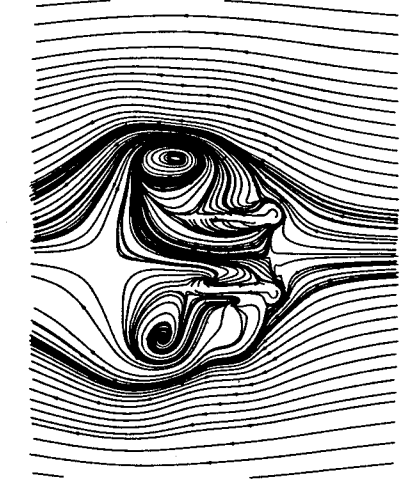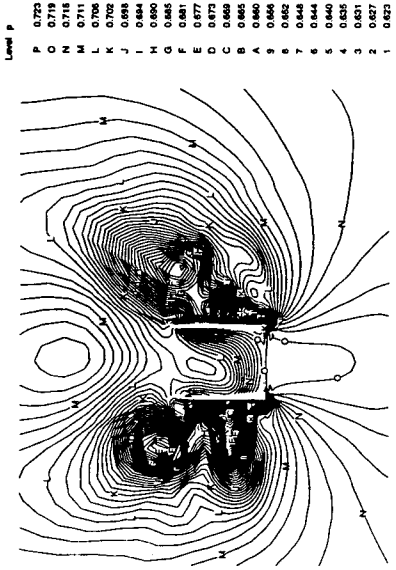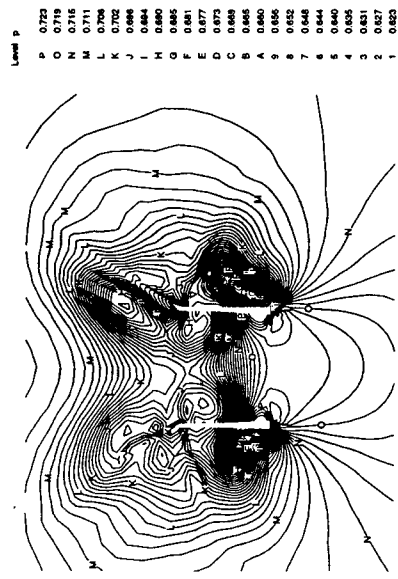
Figure 11: Snap shots of static pressure and instantaneous streamlines in a cross-flow plane, $x = 1.096$. Uncoupled case after $it = 9,600$ (Inboard position).
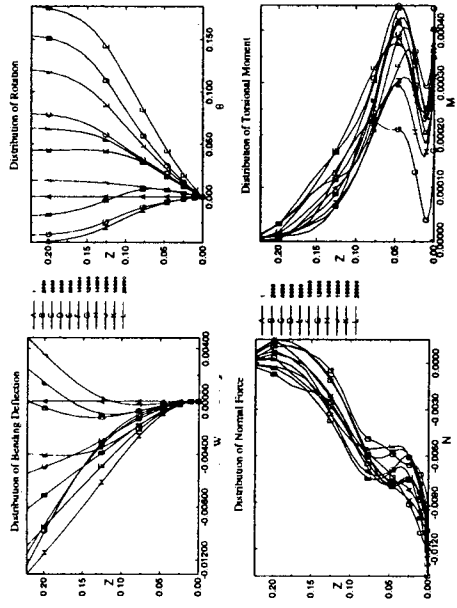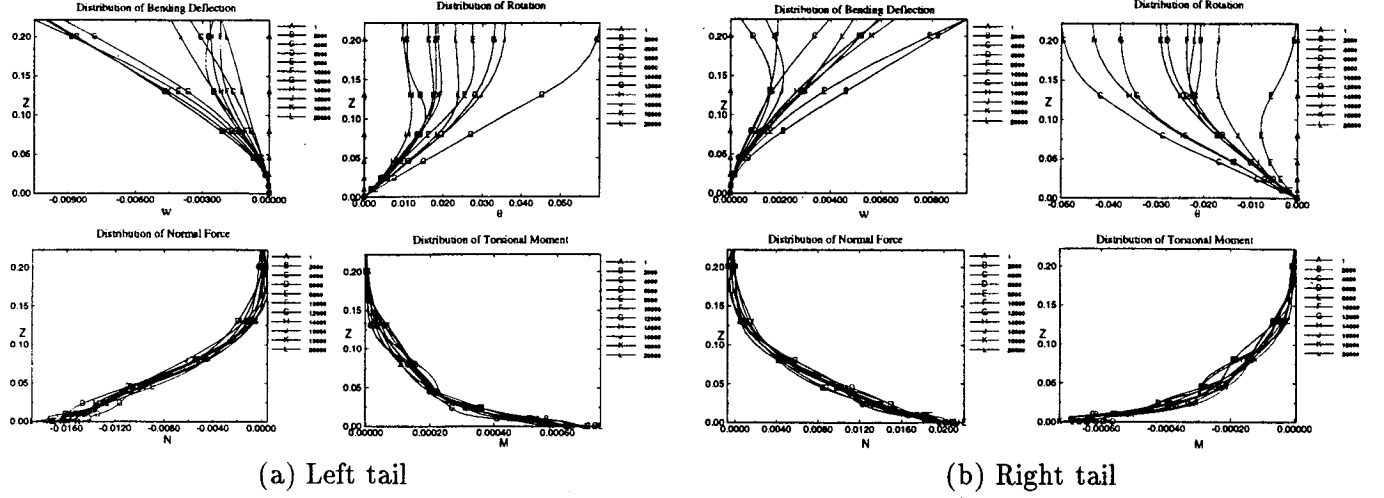
(a) Left tail
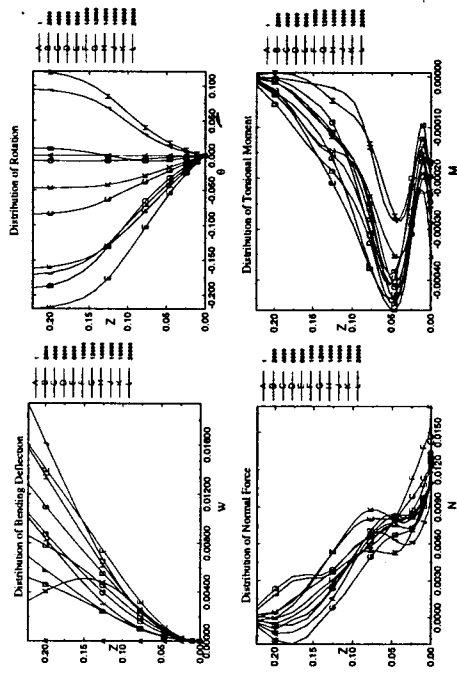
(b) Right tail

Figure 12: Distribution of the deflection and load responses for an uncoupled bending-torsion case. $M_\infty = 0.3$, $\alpha = 30°$, $R_e = 1.25x10^6$, (Inboard position).
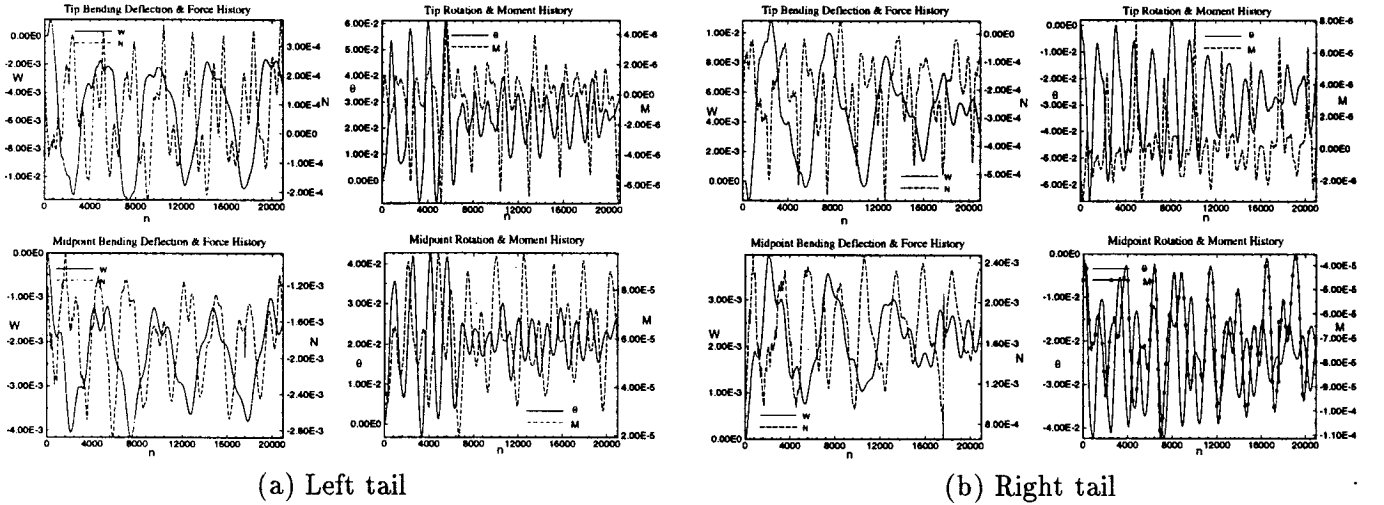
(a) Left tail

(b) Right tail
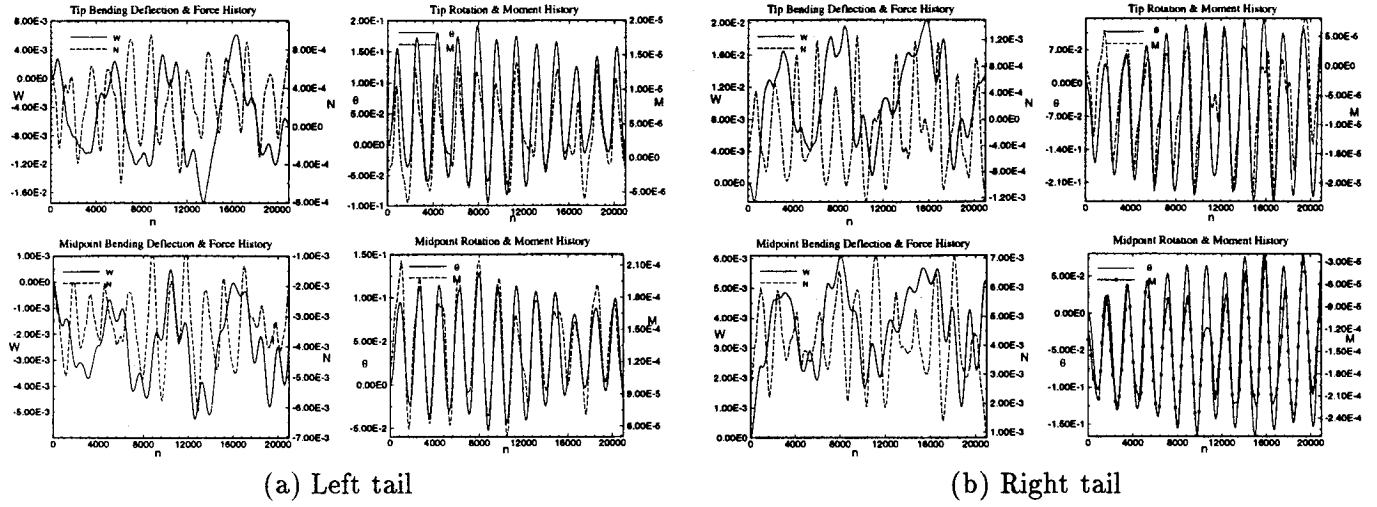
Figure 13: History of the deflection and load responses for an uncoupled bending-torsion case. $M_\infty = 0.3$, $\alpha = 30^o$, $R_e = 1.25x10^6$, (Inboard position).
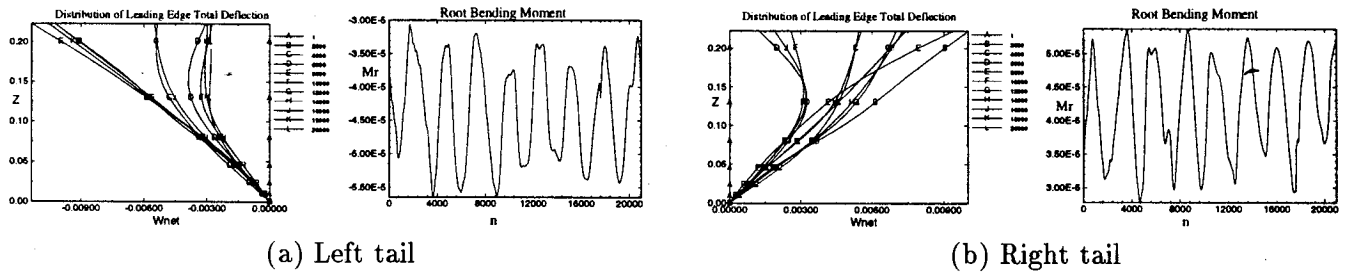

(a) Left tail

(b) Right tail
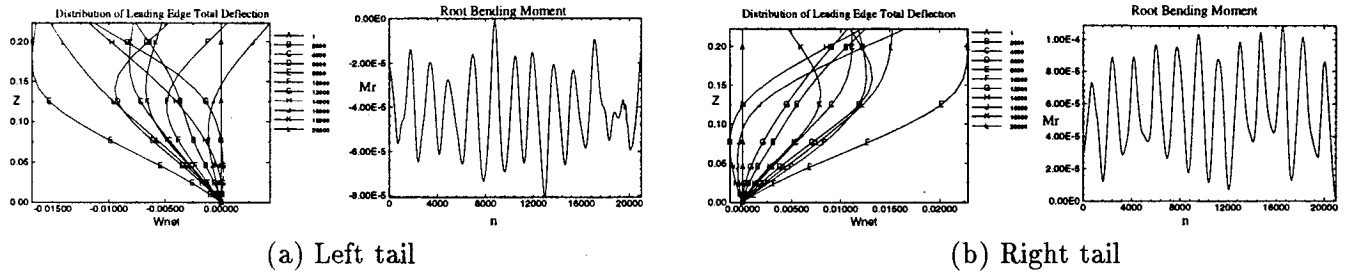
Figure 14: Total structural deflections and root bending moment for an uncoupled bending-torsion case. $M_\infty = 0.3$, $\alpha = 30^o$, $R_e = 1.25x10^6$, (Inboard position).
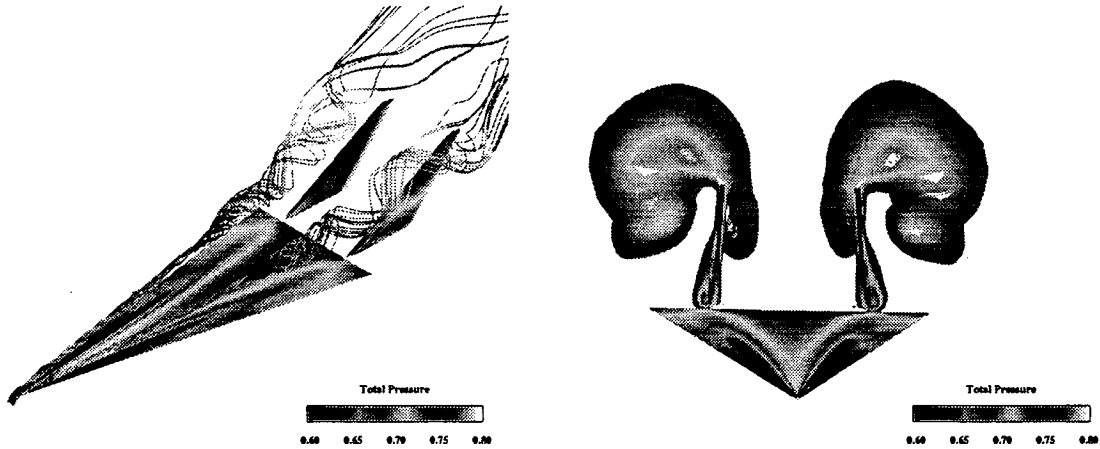
Figure 15: Three-dimensional and front views showing the total pressure on the surfaces, and the vortex-core streamlines. Initial conditions (Midspan position).

Figure 16: Initial conditions for static pressure and instantaneous streamlines in a cross-flow plane, $x = 1.096$ (Midspan position).
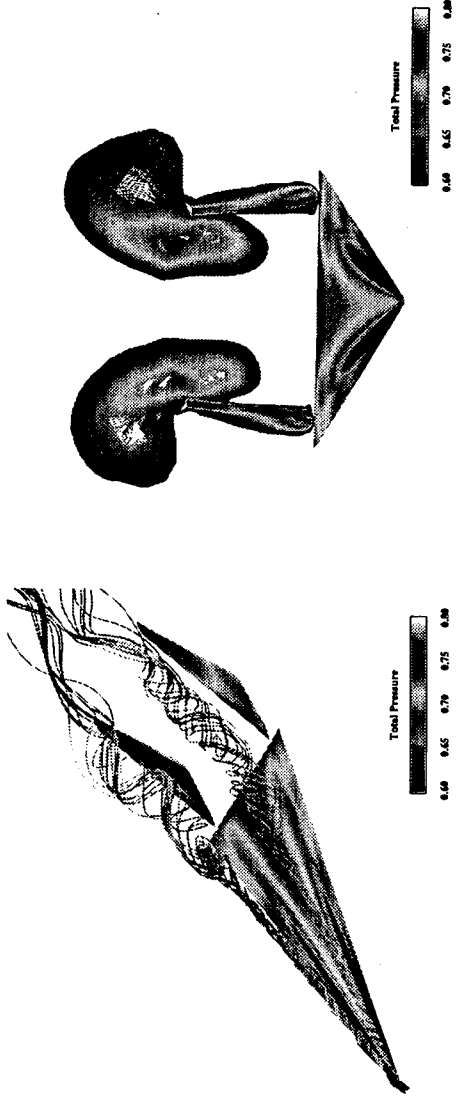

Figure 17: Three-dimensional and front views showing the total pressure on the surfaces, and the vortex-core streamlines. Uncoupled case after $it = 9,600$ (Midspan position).
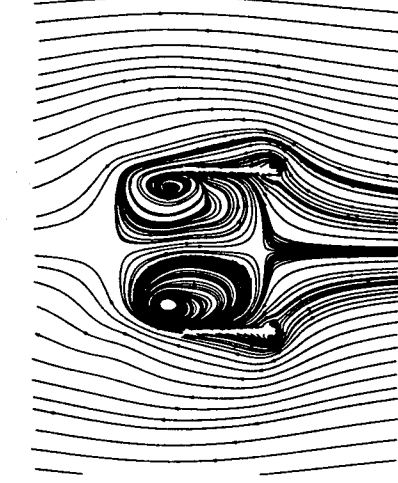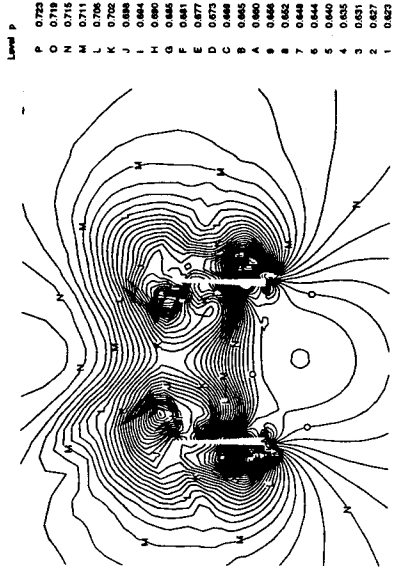

Figure 18: Snap shots of static pressure and instantaneous streamlines in a cross-flow plane, $x = 1.096$. Uncoupled case after $it = 9,600$ (Midspan position).

16

(a) Left tail

(b) Right tail

Figure 19: Distribution of the deflection and load responses for an uncoupled bending-torsion case. $M_\infty = 0.3$, $\alpha = 30°$, $R_e = 1.25x10^6$, (Midspan position).
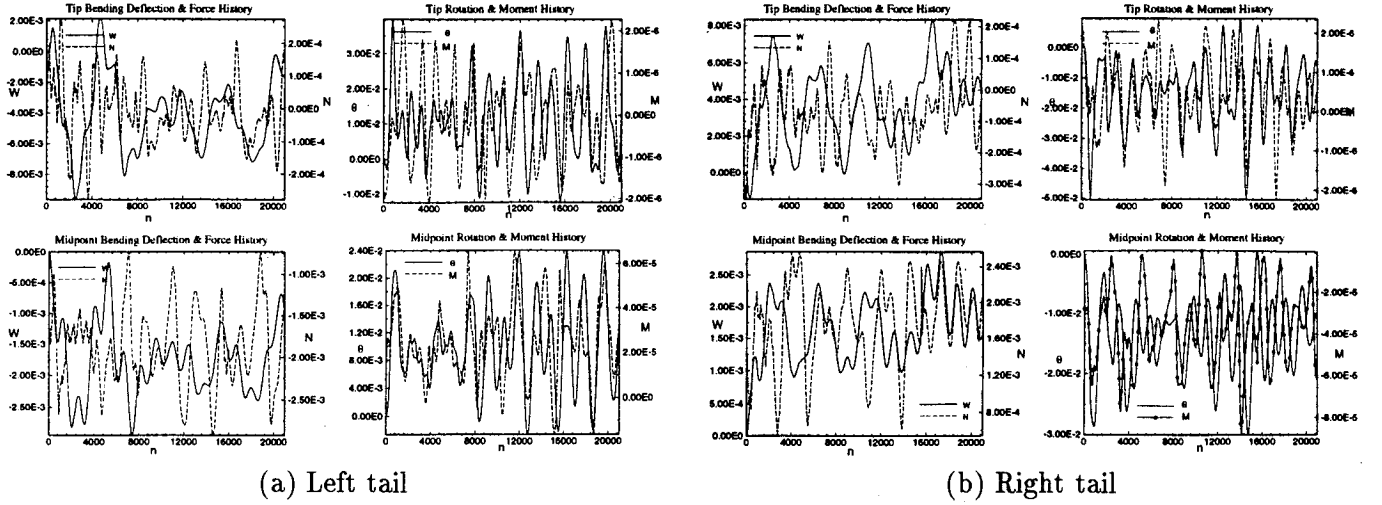

(a) Left tail

(b) Right tail

Figure 20: History of the deflection and load responses for an uncoupled bending-torsion case. $M_\infty = 0.3$, $\alpha = 30°$, $R_e = 1.25x10^6$, (Midspan position).

(a) Left tail

(b) Right tail

Figure 21: Total structural deflections and root bending moment for an uncoupled bending-torsion case. $M_\infty = 0.3$, $\alpha = 30°$, $R_e = 1.25x10^6$, (Midspan position).

Figure 22: Three-dimensional and front views showing the total pressure on the surfaces, and the vortex-core streamlines. Uncoupled case after $it = 9,600$ (Outboard position).

Figure 23: Snap shots of static pressure and instantaneous streamlines in a cross-flow plane, $x = 1.096$. Uncoupled case after $it = 9,600$ (Outboard position).
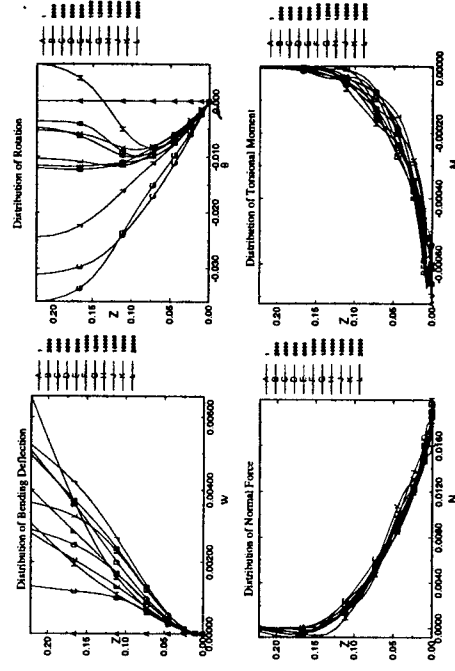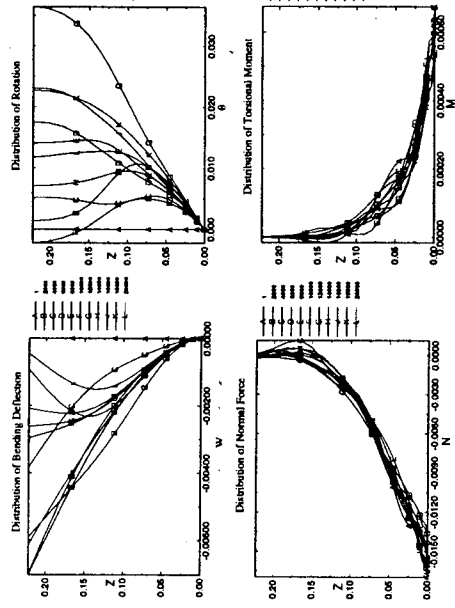
(a) Left tail

(b) Right tail

Figure 24: Distribution of the deflection and load responses for an uncoupled bending-torsion case. $M_\infty = 0.3$, $\alpha = 30°$, $R_e = 1.25x10^6$, (Outboard position).

18

(a) Left tail   (b) Right tail

Figure 25: History of the deflection and load responses for an uncoupled bending-torsion case. $M_\infty = 0.3$, $\alpha = 30^\circ$, $R_e = 1.25x10^6$, (Outboard position).
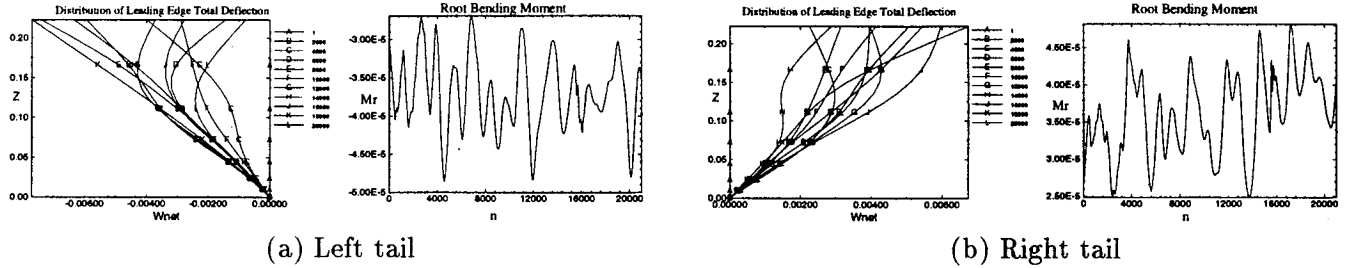

(a) Left tail   (b) Right tail

Figure 26: Total structural deflections and root bending moment for an uncoupled bending-torsion case. $M_\infty = 0.3$, $\alpha = 30^\circ$, $R_e = 1.25x10^6$, (Outboard position).
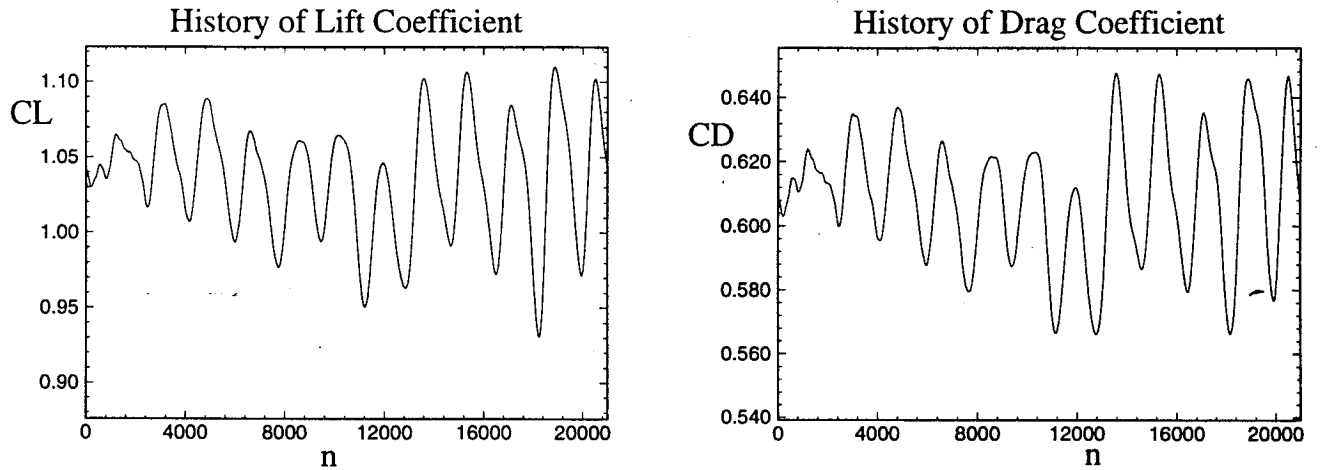

Figure 27: Hisotory of the forces on the wing/twin-tail configuration. $M_\infty = 0.3$, $\alpha = 30^\circ$, $R_e = 1.25x10^6$, (Inboard position).
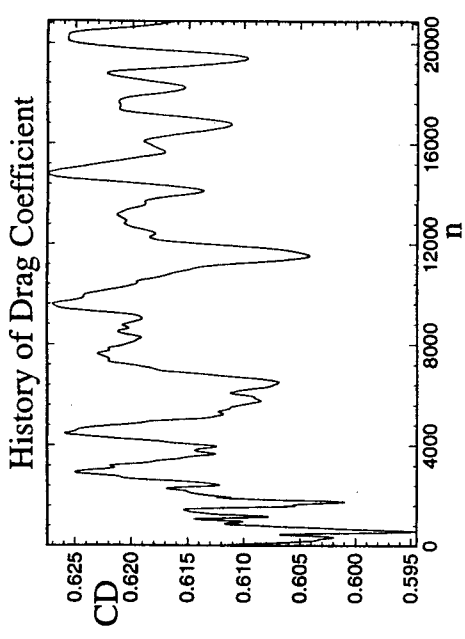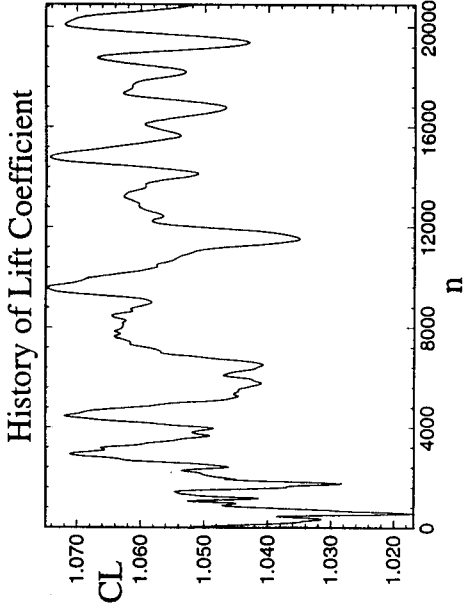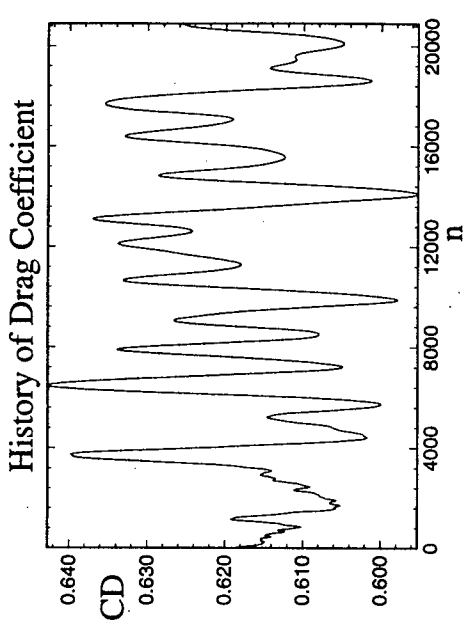
19

Figure 28: History of the forces on the wing/twin-tail configuration. $M_\infty = 0.3$, $\alpha = 30^o$, $R_e = 1.25x10^6$, (Midspan position).
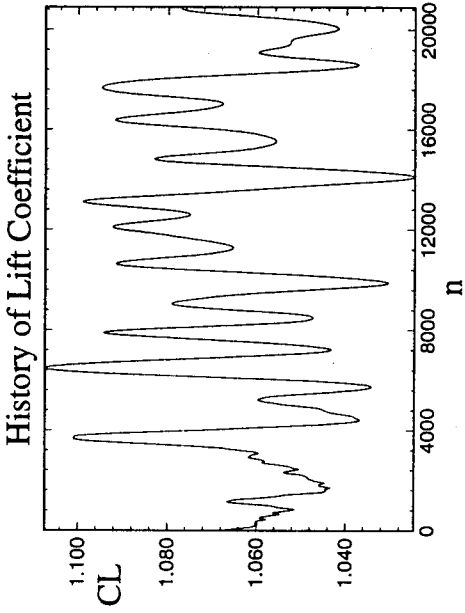

Figure 29: History of the forces on the wing/twin-tail configuration. $M_\infty = 0.3$, $\alpha = 30^o$, $R_e = 1.25x10^6$, (Outboard position).